

Effects of uniform and non-uniform salinity profiles on the onset of double diffusive Rayleigh-Benard convection in a composite system bounded by rigid-rigid boundaries with Soret effects and constant heat sources

¹ Somalatha. M. T. ^{2,*} Archana. M. A., ³ Sumithra. R., ^{4,a} Darshan. B. K., ^{4,b} Gowthami. S.,
^{4,c} Manoj. M. N., ^{4,d} Pavankalyan

^{1,2,3,4} Department of UG, PG Studies and Research in Mathematics,
Government Science College (Autonomous), Bengaluru, Karnataka, India
Corresponding author*: archanamurthy78@gmail.com

Abstract

The onset of double diffusive Rayleigh-Benard (DD-RB) convection in a composite system comprising an incompressible fluid saturated densely packed porous layer over which lies a layer of the same fluid with Soret effect and constant heat sources is investigated. The lower rigid surface of the porous layer and the upper free surface of the fluid layer are insulating to heat and mass. The resulting eigen value problem is solved using regular perturbation technique with wave number as a perturbation parameter. The expression for the critical Rayleigh number is obtained for Linear (LSP), Parabolic (PSP), Inverted parabolic (IPSP), Salted from below (SFB) and step function (SF) salinity profiles. The effects of variation of different dimensionless parameters on the onset of DD-RB convection is discussed.

Keywords: Double diffusive convection, Soret effect, Heat Source, Composite system

1 Introduction

The Soret effect or thermal diffusion is the mass flux that is caused by gradients in temperature. The Soret effect plays a crucial role in modulating the interaction between temperature and solute concentration gradients in DDRB convection. This phenomenon has significant applications across various fields, such as, Saline groundwater transport, Polar ice sheets, heat recovery in geothermal reservoirs, migration of radioactive contaminants, separation process, cellular transport mechanisms, climate modeling, astrophysics and space sciences. Platten and Chavepeyer (1973) have investigated oscillatory motion both theoretically and experimentally in Benard cells resulting from the Soret effect. Caldwell (1976) has investigated thermosolutal convection in a solution with high negative Soret coefficient. The sufficient condition for the coincidence of the linear and nonlinear stability parameters of the stationary state in a thermo-diffusive fluid mixture problem was established by Rionero and Mulone (1987). Examining the Benard convection in binary mixes with the Soret effect, Zimmermann et al. (1992) carried out experiments on amalgams of ethyl alcohol and water. Straughan and Hutter (1999) investigated the structural stability of Soret-induced double-diffusive convection problem. Alex *et al.* (2001) examined the influence of variable gravitational field on Soret-driven thermosolutal convection inside a porous material. The experimental findings of Soret effect was reviewed by Platten (2006). Kaffel *et al.* (2008) provided numerical and analytical investigation of Soret effect on thermohaline convection in a square enclosure containing binary mixture. Deepika (2018) explored how the Soret parameter affects the initiation of double-diffusive convection (DDC) in a fluid-saturated porous layer. Altawallbeh *et al.* (2018) expanded on this research by including local thermal

non-equilibrium, deriving both linear and nonlinear stability criteria. Recently, Sumithra *et al.* (2022) analyzed the impact of thermal diffusion on DDC in a composite system using Darcy-Brinkman-Rayleigh-Benard model. The onset of thermosolutal Marangoni convection in an anisotropic porous layer stacked underneath fluid layer with Soret effect has been investigated by Gangadharaiah (2023). Internal heat sources/sinks are crucial in various fields including engineering, electronics, manufacturing and biology. Applications include thermal management systems using heat sinks, coolers, and active or passive cooling methods, energy harvesting through thermoelectric generators, managing heat in consumer electronics for performance and safety, maintaining temperature-controlled environments in manufacturing, and utilizing internal heat in medical treatments and space exploration. The literature on internal heat source/sink has evolved significantly over the years (Tveitereid (1978), Yu and Shih (1980), Ames and Straughan (1990), Shankar *et al.* (2019)). The unsteady, laminar double-diffusive convection in a isotropic porous rectangular cavity with temperature dependent heat source or sink applying cooperating heat and mass gradient was studied by Chamka (2002). The linear and nonlinear stability assessments of double-diffusive convection in a fluid-saturated porous layer with a concentration-based internal heat source without or with the Soret effect were investigated by Hill (2005) and Israel-Cooke (2018) respectively. The initiation of thermosolutal convective instability in a horizontal porous layer filled with a power-law fluid, which is influenced by concentration-based internal heat sources and the Soret effect, was examined by Kumari and Murthy (2019).

Recent advancement in modern technology have sparked increased interest among researchers in studying transport phenomena in both natural and engineered systems. One area of focus is the investigations of heat and mass transfer within composite systems, where a fluid and a porous medium are both saturated with the same fluid. These studies have gained momentum in recent years due their broad applicability in various natural and industrial processes, including geothermal energy extraction from reservoirs, fumigation of stired grains, cooling of aluminum billets, filtration and so on. The issue of the initiation of finger convection in a porous layer situated beneath a fluid layer has been examined through linear stability analysis by Chen and Chen (1988). Chen and Lu (1991) studied the impact of temperature-dependent viscosity on buoyancy-driven salt-finger convection, identifying two effects: a viscous sublayer that stabilizes through multicellular convection and reduced viscosity that facilitates convection onset. Chen (1992) investigated salt-finger instability in a fluid layer above an anisotropic and inhomogeneous porous medium using linear stability analysis. Al-Qurashi (2012) explored salt-finger convection in a rotating system, showing that non-linearity does not affect stationary instability in a magnetofluid above a porous layer, but significantly impacts overstability. Gangadharaiah (2013) analyzed double diffusive convection with Marangoni instabilities in a fluid-porous structure. The impact of both uniform and non-uniform salinity gradients on the initiation of double-diffusive convection in a composite layer is examined by Komala and Sumithra (2019). Sumithra and Komala (2020) observed how surface tension, magnetic fields, and salinity gradients affect the onset of double-diffusive buoyancy-driven convection in a fluid-porous composite system under a vertical magnetic field.

2 Mathematical Analysis

Consider an infinite horizontal incompressible fluid saturated porous layer of thickness d_m underlying a layer of the same fluid of thickness d with Soret effect and constant heat sources. The upper and lower rigid boundaries are subjected to adiabatic temperature and concentration boundary conditions. A Cartesian coordinate system is chosen such that the origin is at the interface and z-axis vertically upwards. The temperatures of the lower and upper

boundaries are taken as T_L and T_U respectively, with $T_U < T_L$. The solutes of the lower and upper boundaries are taken as C_L and C_U respectively, with $C_U < C_L$. The equations governing the fluid layer are:

$$\nabla \cdot \vec{q}_f = 0 \quad (2.1)$$

$$\rho_0 \left(\frac{\partial \vec{q}_f}{\partial t} + (\vec{q}_f \cdot \nabla) \vec{q}_f \right) = -\nabla P_f + \mu \nabla^2 \vec{q}_f - \rho g \hat{k} \quad (2.2)$$

$$\frac{\partial T_f}{\partial t} + (\vec{q}_f \cdot \nabla) T_f = \kappa_f \nabla^2 T_f + Q_f \quad (2.3)$$

$$\frac{\partial C_f}{\partial t} + (\vec{q}_f \cdot \nabla) C_f = \kappa_c \nabla^2 C_f + \kappa_T \nabla^2 T_f \quad (2.4)$$

$$\rho = \rho_0 [1 - \alpha_T (T_f - T_0) + \alpha_s (C_f - C_0)] \quad (2.5)$$

The equations governing the porous layer are:

$$\nabla_m \cdot \vec{q}_m = 0 \quad (2.6)$$

$$\frac{\rho_0}{\phi} \left(\frac{\partial \vec{q}_m}{\partial t} + (\vec{q}_m \cdot \nabla_m) \vec{q}_m \right) = -\nabla_m P_m - \frac{\mu}{K} \vec{q}_m - \rho_m g \hat{k} \quad (2.7)$$

$$A \frac{\partial T_m}{\partial t} + (\vec{q}_m \cdot \nabla_m) T_m = \kappa_m \nabla_m^2 T_m + Q_m \quad (2.8)$$

$$\phi \frac{\partial C_m}{\partial t} + (\vec{q}_m \cdot \nabla_m) C_m = \kappa_{cm} \nabla_m^2 C_m + \kappa_{mT} \nabla_m^2 T_m \quad (2.9)$$

$$\rho_m = \rho_0 [1 - \alpha_{Tm} (T_m - T_0) + \alpha_{sm} (C_m - C_0)] \quad (2.10)$$

Where $\vec{q}_f = (u_f, v_f, w_f)$ and $\vec{q}_m = (u_m, v_m, w_m)$ are the velocity vectors, μ is the fluid viscosity, P is the total pressure, t is the time, ϕ is the porosity, κ_f and κ_m are respectively the thermal diffusivities of the fluid and porous medium, $A = \frac{(\rho_0 c_p)_m}{(\rho_0 c_p)_f}$ is the ratio of heat capacities,

C_p is the specific heat, T_f and T_m respectively denote the temperatures in the fluid and porous layers. Q_f and Q_m denotes heat sources, K denotes permeability of the porous medium, ρ_0 is the fluid density at the reference temperature T_0 , g is the acceleration due to gravity acting vertically downwards. C_f and C_m are species concentrations in fluid and porous layers respectively, κ_c and κ_{cm} are the solute diffusivities in fluid and porous layers respectively. κ_T and κ_{mT} represents Soret coefficients in fluid and porous layers respectively. The subscripts 'm', 'f' and 's' refer to the porous, fluid and solid mediums respectively.

The basic steady state is assumed to be quiescent, and pressure, concentration, temperature are functions of z only. We consider the solution in the form.

$$\vec{q}_f = \vec{q}_{fb} = \mathbf{0}, P_f = P_{fb}(z_f), C_f = C_{fb}(z_f), T_f = T_{fb}(z_f) \quad (2.11)$$

$$\vec{q}_m = \vec{q}_{mb} = \mathbf{0}, P_m = P_{mb}(z_m), C_m = C_{mb}(z_m), T_m = T_{mb}(z_m) \quad (2.12)$$

The temperature distributions $T_{fb}(z_f)$ and $T_{mb}(z_m)$ are found to be

$$T_{fb}(z_f) = T_0 + \frac{(T_U - T_0)z_f}{d_f} + \frac{Q_f z_f (d_f - z_f)}{2\kappa_f} \quad (2.13)$$

$$T_{mb}(z_m) = T_0 + \frac{(T_0 - T_L)z_m}{d_m} + \frac{Q_m z_m (d_m - z_m)}{2\kappa_m} \quad (2.14)$$

Where the interface temperature T_0 is given by

$$T_0 = \frac{2(\kappa_f T_U d_m + \kappa_m T_L d_f) + Q_f d_f^2 d_m + d_f Q_m d_m^2}{2(\kappa_f d_m + \kappa_m d_f)} \quad (2.15)$$

The concentration distributions C_{fb} and C_{mb} are found to be

$$C_{fb}(z_f) = C_0 + \left[\frac{(C_U - C_0)z_f}{d_f} - \frac{\lambda Q_f z_f (d_f - z_f)}{2} \right] f(z_f) \quad (2.16)$$

$$C_{mb}(z_m) = C_0 + \left[\frac{(C_0 - C_L)z_m}{d_m} - \frac{\lambda_m Q_m z_m (d_m - z_m)}{2} \right] f_m(z_m) \quad (2.17)$$

where $f(z_f)$ and $f_m(z_m)$ are dimensionless gradient functions, and C_0 , the interface concentration is given by

$$C_0 = \frac{2(d_m \kappa_c C_U + d_f \kappa_m C_L) - \lambda \kappa_c Q_f d_m d_f^2 - d_f \kappa_{mc} \lambda_m Q_m d_m^2}{(\kappa_f d_m + \kappa_m d_f)} \quad (2.18)$$

To investigate the stability analysis of the basic solution, perturbations are superimposed in the form:

$$\vec{q}_f = \vec{q}_{fb} + \vec{q}_f', \mathbf{P}_f = \mathbf{P}_{fb}(z_f) + \mathbf{P}_f', \mathbf{C}_f = \mathbf{C}_{fb}(z_f) + \mathbf{s}_f, \mathbf{T}_f = \mathbf{T}_{fb}(z_f) + \boldsymbol{\theta}_f \quad (2.19)$$

$$\left. \begin{aligned} \vec{q}_m &= \vec{q}_{mb} + \vec{q}_m', \mathbf{P}_m = \mathbf{P}_{mb}(z_m) + \mathbf{P}_m', \mathbf{C}_m = \mathbf{C}_{mb}(z_m) + \mathbf{s}_m, \\ \mathbf{T}_m &= \mathbf{T}_{mb}(z_m) + \boldsymbol{\theta}_m \end{aligned} \right\} \quad (2.20)$$

The above equations are substituted in equations (2.1) to (2.10) and linearized in the usual manner. By taking curl twice on equations (2.2) and (2.7), the pressure terms are eliminated, only the vertical components are retained. Separate length scales are used for the fluid and porous layers in order to render the equations non-dimensional, ensuring that both layers have a unit depth and are:

$$\left. \begin{aligned} (\mathbf{u}_f, \mathbf{v}_f, \mathbf{w}_f) &= \frac{\kappa_f}{d_f} (\mathbf{u}_f^*, \mathbf{v}_f^*, \mathbf{w}_f^*), \boldsymbol{\theta}_f = (T_0 - T_U)\boldsymbol{\theta}_f^*, \mathbf{t}_f = \frac{d_f^2}{\kappa_f} \mathbf{t}_f^*, \nabla_f = \frac{\nabla_f^*}{d_f}, \\ (x_f, y_f, z_f) &= d_f(x_f^*, y_f^*, z_f^*), \mathbf{s}_f = (C_0 - C_U)\mathbf{s}_f^* \end{aligned} \right\} \quad (2.21)$$

$$\left. \begin{aligned} (\mathbf{u}_m, \mathbf{v}_m, \mathbf{w}_m) &= \frac{\kappa_m}{d_m} (\mathbf{u}_m^*, \mathbf{v}_m^*, \mathbf{w}_m^*), \boldsymbol{\theta}_m = (T_L - T_0)\boldsymbol{\theta}_m^*, \mathbf{t}_m = \frac{d_m^2}{\kappa_m} \mathbf{t}_m^*, \\ \nabla_m &= \frac{\nabla_m^*}{d_m}, (x_m, y_m, z_m) = d_m(x_m^*, y_m^*, z_m^* - 1), \mathbf{s}_m = (C_L - C_0)\mathbf{s}_m^* \end{aligned} \right\} \quad (2.22)$$

The linearized non-dimensional equations are:

$$\frac{1}{Pr_f} \frac{\partial (\nabla_f^2 \mathbf{w}_f)^2}{\partial \mathbf{t}_f} = \nabla_f^4 \mathbf{w}_f + Ra_T \nabla_{2f}^2 \boldsymbol{\theta}_f - Ra_S \nabla_{2f}^2 \mathbf{s} \quad (2.23)$$

$$\frac{\partial \boldsymbol{\theta}_f}{\partial \mathbf{t}_f} - \mathbf{w}_f - Q_f \frac{(2z_f - 1)d_f^2 \mathbf{w}_f}{2\kappa_f(T_0 - T_U)} = \nabla_f^2 \boldsymbol{\theta}_f \quad (2.24)$$

$$\frac{\partial s_f}{\partial t_f} - w_f + \frac{\lambda Q_f d_f^2 (2z_f - 1) w_f}{2(C_0 - C_U)} = \tau_f \nabla_f^2 s + \tau_T \frac{(T_0 - T_U)}{(C_0 - C_U)} \nabla_f^2 \theta_f \quad (2.25)$$

$$\frac{\beta^2}{Pr_m} \frac{\partial w_m}{\partial t_m} = -\nabla_m^2 w_m + Ra_m \nabla_m^2 \theta_m - Ra_{sm} \nabla_m^2 s_m \quad (2.26)$$

$$A \frac{\partial \theta_m}{\partial t_m} - w_m \frac{Q_m (2z_m + 1)}{2\kappa_m (T_L - T_0)} = \nabla_m^2 \theta_m \quad (2.27)$$

$$\phi \frac{\partial s_m}{\partial t_m} - w_m + \frac{\lambda_m Q_m d_m^2 (2z_m - 1) w_m}{2(C_L - C_0)} = \tau_c \nabla_m^2 s_m + \tau_{cT} \frac{(T_0 - T_U)}{(C_0 - C_U)} \nabla_m^2 \theta_m \quad (2.28)$$

where $Pr_f = \frac{\mu}{\rho_0 \kappa_f}$, $\beta^2 = Da = \frac{K}{d_m^2}$, $Ra_T = \frac{\alpha_f g (T_0 - T_U)}{\nu \kappa_f}$, $Pr_m = \frac{\phi \nu}{\kappa_m}$, $Ra_m = \frac{\alpha_m g (T_L - T_0) d_m K}{\nu_m \kappa_m}$, $Ra_s = \frac{g \alpha_s (C_0 - C_U) d_f^3}{\nu \kappa_c}$, $Ra_{sm} = \frac{\alpha_{sm} g (C_L - C_0) d_m^3}{\nu_m \kappa_{cm}}$ are Prandtl number in fluid layer, Darcy number, thermal Rayleigh number in fluid layer, Prandtl number in porous layer, thermal Rayleigh number in porous layer, solute Rayleigh number in fluid layer, and solute Rayleigh number in porous layer. Here $\nu = \frac{\mu}{\rho_0}$ and ν_m is effective viscosity in porous layer.

Normal Mode Expansion

Carrying out the following normal mode analysis on the dimensionless equations, the

$$\begin{bmatrix} w_f \\ \theta_f \\ s_f \end{bmatrix} = \begin{bmatrix} W_f(z_f) \\ \Theta_f(z_f) \\ S_f(z_f) \end{bmatrix} g(x_f, y_f) e^{\eta_f t_f} \quad (2.29)$$

$$\begin{bmatrix} w_m \\ \theta_m \\ s_m \end{bmatrix} = \begin{bmatrix} W_f(z_m) \\ \Theta_f(z_m) \\ S_f(z_m) \end{bmatrix} g_m(x_m, y_m) e^{\eta_m t_m} \quad (2.30)$$

Subsequent ordinary differential equations obtained are:

$$(D_f^2 - a_f^2)^2 W_f(z_f) + \frac{\eta_f}{Pr_f} (D_f^2 - a_f^2) W_f(z_f) \quad (2.31)$$

$$= a_f^2 [Ra_T \Theta_f(z_f) - Ra_s S_f(z_f)]$$

$$\left((D_f^2 - a_f^2) + \eta_f \right) \Theta_f(z_f) + W_f(z_f) + \frac{Q_f d_f^2 (2z_f - 1)}{2\kappa_f (T_0 - T_U)} W_f(z_f) = 0 \quad (2.32)$$

$$\left. \begin{aligned} (\tau_f (D_f^2 - a_f^2) + \eta_f) S_f(z_f) f(z_f) + \frac{Q_f \lambda d_f^2 (2z_f - 1)}{2\kappa_f (C_0 - C_U)} W_f(z_f) \\ + W_f(z_f) + Sr_f (D_f^2 - a_f^2) \Theta_f(z_f) \end{aligned} \right\} = 0 \quad (2.33)$$

$$\left[\frac{\beta^2}{Pr_m} - 1 \right] (D_m^2 - a_m^2) W_m(z_m) = a_m^2 [Ra_m \Theta_m(z_m) - Ra_{sm} S_m(z_m)] \quad (2.34)$$

$$\left((D_m^2 - a_m^2) + \phi \eta_m \right) \Theta_m(z_m) + W_m(z_m) + \frac{Q_m d_m^2 (2z_m + 1)}{2\kappa_m (T_L - T_0)} W_m(z_m) = 0 \quad (2.35)$$

$$\left. \begin{aligned} &(\tau_m(D_m^2 - a_m^2) + \phi\eta_m)S_m(z_m)f_m(z_m) - \frac{Q_m\lambda_m d_m^2(2z_m + 1)}{2\kappa_m(C_0 - C_U)}W_m(z_m) \\ &+ W_m(z_m) + Sr_m(D_m^2 - a_m^2)\Theta_m(z_m) \end{aligned} \right\} = 0 \quad (2.36)$$

Where $\lambda = \frac{R_f^* Sr_f}{\tau_f}$ and $\lambda_m = \frac{R_{Im}^* Sr_m}{\tau_m}$

Since the principle of exchange of stability holds for the given problem, time derivatives are neglected. That is, $\eta_f = \eta_m = 0$. Thus, the convection manifests itself as stationary convection directly, and the equations (2.31) to (2.36) reduces to the following form:

$$(D_f^2 - a_f^2)^2 W_f(z_f) = a_f^2 [Ra_T \Theta_f(z_f) - Ra_S S_f(z_f)] \quad (2.37)$$

$$(D_f^2 - a_f^2)\Theta_f(z_f) + W_f(z_f) + R_f^*(2z_f - 1)W_f(z_f) = 0 \quad (2.38)$$

$$\left. \begin{aligned} &(D_f^2 - a_f^2)S_f(z_f)f(z_f) + \frac{1}{\tau_f}[1 + \lambda(2z_f - 1)]W_f(z_f) \\ &+ Sr_f(D_f^2 - a_f^2)\Theta_f(z_f) \end{aligned} \right\} = 0 \quad (2.39)$$

$$(D_m^2 - a_m^2)W_m(z_m) = a_m^2 [Ra_m \Theta_m(z_m) - Ra_{Sm} S_m(z_m)] \quad (2.40)$$

$$(D_m^2 - a_m^2)\Theta_m(z_m) + W_m(z_m) + R_{Im}^*(2z_m + 1)W_m(z_m) = 0 \quad (2.41)$$

$$\left. \begin{aligned} &(D_m^2 - a_m^2)S_m(z_m)f_m(z_m) + \frac{1}{\tau_m}[1 - \lambda_m(2z_m + 1)]W_m(z_m) \\ &+ Sr_m(D_m^2 - a_m^2)\Theta_m(z_m) \end{aligned} \right\} = 0 \quad (2.42)$$

where $R_f^* = \frac{Q_f d_f^2}{2\kappa_f(T_0 - T_U)}$ and $R_{Im}^* = \frac{Q_m d_m^2}{2\kappa_m(T_L - T_0)}$ are respectively modified internal Rayleigh numbers in fluid and porous layers, $Sr_f = \frac{\tau_T(T_0 - T_U)}{\tau_f(C_0 - C_U)}$ and $Sr_m = \frac{\tau_{CT}(T_L - T_0)}{\tau_m(C_L - C_0)}$ are respectively Soret parameters in fluid and porous layers. D_f and D_m are differential operators with respect to z_f and z_m . If the matching of the solution in the two layers is possible, the wave number must be the same for the fluid and porous layer, so that we have $\frac{a_f}{a_m} = \frac{d_f}{d_m}$

Boundary conditions

To solve the equations (2.37) to (2.42), we impose the following boundary conditions (after implementing non-dimensionalization and normal mode analysis).

Velocity boundary conditions are:

$$\left. \begin{aligned} &W_f(1) = 0; D_f W_f(1) = 0; \epsilon_T \hat{d} W_f(0) = W_m(1); D_m W_m(0) = 0 \\ &\hat{d}^3 \epsilon_T (D_f^2 + a_f^2) W_f(0) = (D_m^2 + a_m^2) W_m(1); \\ &\hat{d}^4 \epsilon_T D a (D_f^3 - 3a_f^2 D_f) W_f(0) + D_m W_m(1) = 0 \end{aligned} \right\} \quad (2.43)$$

Temperature boundary conditions are:

$$D_f \Theta_f(1) = 0; \Theta_f(0) = \hat{d} \epsilon_T \Theta_m(1); D_f \Theta_f(0) = D_m \Theta_m(1); D_m \Theta_m(0) = 0 \quad (2.44)$$

Salinity boundary conditions are:

$$D_f S_f(1) = 0; S_f(0) = \hat{d} \epsilon_s S_m(1); D_f S_f(0) = D_m S_m(1); D_m S_m(0) = 0 \quad (2.45)$$

where $\hat{d} = \frac{d_m}{d_f}$ is the depth ratio, $\epsilon_T = \frac{\kappa_f}{\kappa_m}$ is thermal diffusivity ratio, $\epsilon_s = \frac{\kappa_c}{\kappa_{cm}}$ is solute diffusivity ratio.

3 Solution by regular perturbation technique:

To validate tiny wave number analysis, the dependent variables in both fluid and porous layers are presented in powers of a_f^2 , as follows:

$$(W_f(z_f), \Theta_f(z_f), S_f(z_f)) = \sum_{i=0}^{\infty} (a_f^2)^i (W_{fi}(z_f), \Theta_{fi}(z_f), S_{fi}(z_f)) \quad (3.1)$$

$$(W_m(z_m), \Theta_m(z_m), S_m(z_m)) = \sum_{i=0}^{\infty} (\hat{d}^2 a_f^2)^i (W_{mi}(z_m), \Theta_{mi}(z_m), S_{mi}(z_m)) \quad (3.2)$$

Substituting the above equations into equations (2.37) to (2.42) yields a sequence of equations for the unknown functions $(W_{fi}(z_f), \Theta_{fi}(z_f), S_{fi}(z_f))$ and $(W_{mi}(z_m), \Theta_{mi}(z_m), S_{mi}(z_m))$ for $i = 0, 1, 2, 3, \dots$

The solutions to zeroth order equations satisfying zeroth order boundary conditions are:

$$\left. \begin{aligned} W_{f_0}(z_f) = 0 = W_{m_0}(z_m), \Theta_{f_0}(z_f) = \hat{d}\epsilon_T, \\ \Theta_{m_0}(z_m) = 1, S_{f_0}(z_f) = \hat{d}\epsilon_s, S_{m_0}(z_m) = 1 \end{aligned} \right\} \quad (3.3)$$

The solutions of the velocity equations (2.37) and (2.40) of order a_f^2 , satisfying corresponding boundary conditions (2.43) of the same order are:

$$W_{f_1}(z_f) = F_5 + F_6 z_f + F_7 z_f^2 + F_8 z_f^3 + \frac{\hat{d} z_f^4}{24} (\epsilon_T Ra_T - \epsilon_s Ra_S) \quad (3.4)$$

$$W_{m_1}(z_m) = F_9 + F_{10} z_m + \frac{z_m^2}{2} (Ra_m + Ra_{Sm}) \quad (3.5)$$

where $F_6 = -2F_7 - \frac{\hat{d}}{6} (\epsilon_T Ra_T - \epsilon_s Ra_S) - 3F_8$, $F_7 = \frac{1}{2\hat{d}\epsilon_T} (Ra_m + Ra_{Sm})$, $F_{10} = 0$, $F_8 = -\frac{(Ra_m + Ra_{Sm})}{6\hat{d}^2 \epsilon_T Da}$, $F_5 = F_7 + 2F_8 + \frac{\hat{d}(\epsilon_T Ra_T - \epsilon_s Ra_S)}{8}$, $F_9 = \epsilon_T F_5 - \frac{\hat{d}(Ra_m + Ra_{Sm})}{2}$

The boundary conditions (2.45) and differential equations for concentration (2.39) and (2.42) of order a_f^2 establish the following solvability condition:

$$\begin{aligned} \frac{1}{\tau_f} \int_0^1 [1 + \lambda(2z_f - 1)W_{f_1}(z_f)f(z_f) dz_f] \\ + \frac{\hat{d}^2}{\tau_m} \int_0^1 [1 + \lambda_m(2z_m + 1)W_{m_1}(z_m)f_m(z_m) dz_m] = \hat{d} + \hat{d}\epsilon_s \end{aligned} \quad (3.6)$$

Equation (3.6) is solved for the following salinity gradient functions:

Salinity profile	Gradient function	Critical Rayleigh number
Linear (LSP)	$f(z_f) = 1, f_m(z_m) = 1$	Ra_{T1}
Parabolic (PSP)	$f(z_f) = 2z_f, f_m(z_m) = 2z_m$	Ra_{T2}
Inverted Parabolic (IPSP)	$f(z_f) = 2(z_f - 1),$ $f_m(z_m) = 2(z_m - 1)$	Ra_{T3}

Salted from below (SFBP)	$f(z_f) = \begin{cases} \varepsilon^{-1} & 0 \leq z_f < \varepsilon \\ 0 & \varepsilon < z_f \leq 1 \end{cases}$ $f_m(z_m) = \begin{cases} \varepsilon_m^{-1} & 0 \leq z_m < \varepsilon_m \\ 0 & \varepsilon_m < z_m \leq 1 \end{cases}$	Ra_{T4}
Step function (SFP)	$f(z_f) = \delta(z_f - \varepsilon)$ $f_m(z_m) = \delta_m(z_m - \varepsilon_m)$	Ra_{T5}

3.1 Linear Salinity Profile (LSP):

$$Ra_{T1} = \frac{\hat{d}(\varepsilon_s + Sr_f \varepsilon_T) + \hat{d}^2(1 + Sr_m) - B_{s1} - B_{sm1}}{B_{T1} + B_{m1}}$$

3.2 Parabolic Salinity Profile (PSP):

$$Ra_{T2} = \frac{\hat{d}(\varepsilon_s + Sr_f \varepsilon_T) + \hat{d}^2(1 + Sr_m) - B_{s2} - B_{sm2}}{B_{T2} + B_{m2}}$$

3.3 Inverted Parabolic Salinity Profile (IPSP):

$$Ra_{T3} = \frac{\hat{d}(\varepsilon_s + Sr_f \varepsilon_T) + \hat{d}^2(1 + Sr_m) - B_{s3} - B_{sm3}}{B_{T3} + B_{m3}}$$

3.4 Salted from Below Salinity Profile (SFBP):

$$Ra_{T4} = \frac{\hat{d}(\varepsilon_s + Sr_f \varepsilon_T) + \hat{d}^2(1 + Sr_m) - A_{s4} - A_{sm4}}{A_{T4} + A_{m4}}$$

3.5 Step Function Salinity Profile (SFP):

$$Ra_{T5} = \frac{\hat{d}(\varepsilon_s + Sr_f \varepsilon_T) + \hat{d}^2(1 + Sr_m) - A_{s6} - A_{sm6}}{A_{T6} + A_{m6}}$$

Where $B_{T1} = \frac{1}{\tau_f} \left\{ C_{T4} + C_{T3} \left(\frac{3+\lambda}{6} \right) + C_{T1} \left(\frac{2+\lambda}{6} \right) - C_{T2} \left(\frac{5+3\lambda}{20} \right) + \frac{\hat{d}\varepsilon_T}{360} \right\}$, $C_{T1} = \frac{\varepsilon_T \hat{d}}{12} + \frac{Da \hat{d}^3 \varepsilon_T}{6}$
 $B_{sm1} = \frac{\hat{d}^2}{\tau_m} \left(-C_{s5} (1 - 2\lambda_m) + \frac{(2-5\lambda_m) Ra_{sm}}{12} \right)$, $B_{m1} = \frac{\hat{d}^2}{\tau_m} \left(C_{T5} (1 - 2\lambda_m) + \frac{\varepsilon_T^2 \hat{d}^4 Da}{12} \right)$,
 $B_{s1} = \frac{1}{\tau_f} \left\{ -C_{s4} + C_{s3} \left(\frac{3+\lambda}{6} \right) + C_{s1} \left(\frac{2+\lambda}{6} \right) - C_{s2} \left(\frac{5+3\lambda}{20} \right) \right\}$, $C_{s1} = \frac{Ra_s \varepsilon_s \hat{d}}{12} - \frac{Ra_{sm}}{6 \hat{d} \varepsilon_T}$,
 $B_{T2} = \frac{2}{\tau_f} \left\{ C_{T4} \left(\frac{3-\lambda}{6} \right) + \frac{C_{T3}}{6} + C_{T1} \left(\frac{5+3\lambda}{20} \right) - C_{T2} \left(\frac{3+2\lambda}{15} \right) - \frac{(7+5\lambda) \hat{d} \varepsilon_T}{1008} \right\}$, $C_{s3} = \frac{Ra_{sm}}{2 \hat{d} \varepsilon_T}$
 $B_{m2} = \frac{\hat{d}^2}{\tau_m} \left(C_{T5} \frac{(3-7\lambda_m)}{6} + \frac{(5-13\lambda_m) \varepsilon_T^2 \hat{d}^4 Da}{40} \right)$, $B_{sm2} = \frac{2 \hat{d}^2}{\tau_m} \left(-C_{s5} \frac{(3-7\lambda_m)}{6} + \frac{(5-13\lambda_m) Ra_{sm}}{40} \right)$,
 $B_{s2} = \frac{2}{\tau_f} \left\{ -C_{s4} \left(\frac{3+\lambda}{6} \right) + C_{s3} \left(\frac{2+\lambda}{6} \right) + C_{s1} \left(\frac{5+3\lambda}{20} \right) - C_{s2} \left(\frac{3+2\lambda}{15} \right) - \frac{(7+5\lambda) \hat{d} \varepsilon_s Ra_s}{1008} \right\}$, $C_{T3} = \frac{Da \hat{d}^3 \varepsilon_T}{2}$,
 $B_{T3} = \frac{2}{\tau_f} \left\{ C_{T4} \left(\frac{3-\lambda}{6} \right) + \frac{C_{T3}}{6} + C_{T1} \left(\frac{5+\lambda}{60} \right) - C_{T2} \left(\frac{3+\lambda}{60} \right) + \frac{(7+3\lambda) \hat{d} \varepsilon_T}{5040} \right\}$,
 $B_{m3} = \frac{2 \hat{d}^2}{\tau_m} \left(C_{T5} \frac{(3-5\lambda_m)}{6} + \frac{(5-11\lambda_m) \varepsilon_T^2 \hat{d}^4 Da}{60} \right)$, $B_{sm3} = \frac{2 \hat{d}^2}{\tau_m} \left(-C_{s5} \frac{(3-5\lambda_m)}{6} + \frac{(5-11\lambda_m) Ra_{sm}}{40} \right)$,
 $A_{T4} = \frac{1}{\tau_f} \left\{ C_{T4} H_1 + C_{T3} H_2 + C_{T1} H_3 - C_{T2} H_4 + \frac{\hat{d} \varepsilon_T}{24} H_5 \right\}$, $C_{T2} = Da \hat{d}^2 \varepsilon_T (6C_{T1} - \hat{d}^2 \varepsilon_T)$,
 $A_{m4} = \frac{\hat{d}^2}{\varepsilon_T \tau_m} \left(C_{T5} H_{m2} + \frac{\varepsilon_T^2 \hat{d}^4 Da}{2} H_{m3} \right)$, $A_{sm4} = \frac{\hat{d}^2}{\varepsilon_m \tau_m} \left(-C_{s5} H_{m2} + \frac{Ra_{sm}}{2} H_{m3} \right)$,
 $A_{s4} = \frac{1}{\varepsilon \tau_f} \left\{ C_{s3} H_2 + C_{s1} H_3 + C_{s2} H_4 - C_{s4} H_1 - \frac{\hat{d} \varepsilon_s Ra_s}{24} H_5 \right\}$, $H_1 = \varepsilon [1 + \lambda(\varepsilon - 1)]$,

$$\begin{aligned}
 H_2 &= \varepsilon^2 \left[\frac{1}{2} + \frac{\lambda}{6} (4\varepsilon - 3) \right], H_3 = \varepsilon^3 \left[\frac{1}{3} + \frac{\lambda}{6} (3\varepsilon - 2) \right], H_4 = \varepsilon^4 \left[\frac{1}{4} + \frac{\lambda}{20} (8\varepsilon - 5) \right], \\
 H_5 &= \varepsilon^5 \left[\frac{1}{5} + \frac{\lambda}{15} (5\varepsilon - 3) \right], H_{m1} = \varepsilon_m [1 - \lambda_m (\varepsilon_m + 1)], H_{m2} = \varepsilon_m^2 \left[\frac{1}{2} - \frac{\lambda_m}{6} (4\varepsilon_m + 3) \right], \\
 H_{m3} &= \varepsilon_m^3 \left[\frac{1}{6} + \frac{\lambda_m}{6} (3\varepsilon_m + 1) \right], G = (1 - \lambda + 2\lambda\varepsilon), G_m = (1 - \lambda_m - 2\lambda_m\varepsilon_m), \\
 A_{m6} &= \frac{G_m \hat{d}^2}{\tau_m} \left\{ C_{T5} \varepsilon_m + \frac{\varepsilon_T^2 \hat{d}^4 Da}{2} \varepsilon_m^2 \right\}, A_{T6} = \frac{G}{\tau_f} \left\{ C_{T4} + C_{T3} \varepsilon + C_{T1} \varepsilon^2 - C_{T2} \varepsilon^3 + \frac{\varepsilon^4 \hat{d} \varepsilon_T}{24} \right\}, \\
 A_{sm6} &= \frac{G_m \hat{d}^2}{\tau_m} \left\{ -C_{S5} + \frac{Ra_{sm}}{2} \varepsilon_m^2 \right\}, A_{S6} = \frac{G}{\tau_f} \left\{ C_{S1} \varepsilon^2 + C_{S3} \varepsilon - C_{S4} - C_{S2} \varepsilon^3 + \frac{\varepsilon^4 \hat{d} \varepsilon_S Ra_S}{24} \right\} \\
 C_{S2} &= - (6Da \hat{d}^2 \varepsilon_T C_{S1} + Ra_{sm}), C_{S4} = \frac{\hat{d}}{2\varepsilon_T} (2C_{S2} + Ra_{sm}), C_{T4} = \frac{\hat{d} C_{S2}}{\varepsilon_T} + \frac{\hat{d} \varepsilon_T Da}{2}, \\
 C_{S5} &= C_{S1} + C_{S3} + C_{S4} - \frac{\varepsilon_S \hat{d} Ra_S}{24}, C_{T5} = C_{T4} + C_{T3} - C_{T1} + \frac{\varepsilon_T \hat{d}}{24}
 \end{aligned}$$

4 Results and discussion

The effects of uniform and nonuniform salinity gradients on the onset of double diffusive Rayleigh-Benard convection in a composite system with soret effect and constant heat sources is investigated for rigid-rigid velocity boundary conditions. The Critical Rayleigh numbers (CRN) Ra_{T1} , Ra_{T2} , Ra_{T3} , Ra_{T4} and Ra_{T5} are obtained respectively for Linear (LSP), Parabolic (PSP), Inverted Parabolic (IPSP) salinity profiles in terms of depth ratio \hat{d} , and salted from below (SFBP), step function (SFP) salinity profiles in terms of saline depth ε . In all the graphs considered below i.e., from (4.2) to (4.10), and (4.12) to (4.18), red curve is for the least value, followed by blue, green, cyan and finally, black curve, is for the highest value of the varying parameter.

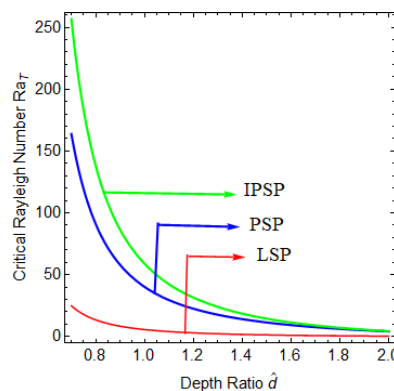


Figure 4.1: Comparison of CRN versus \hat{d} for LSP, PSP and IPSP

Figure 4.1 represents comparison of Linear (LSP), Parabolic (PSP) and Inverted Parabolic (IPSP) salinity profiles for critical Rayleigh number (CRN) versus depth ratio \hat{d} , for the default parameters $R_l^* = R_{lm}^* = 0.5$, $Da = 0.3$, $\varepsilon_T = \varepsilon_S = 1$, $Ra_S = 5$, $Sr_f = Sr_m = -0.1$, $\tau_f = \tau_m = 0.25$. From figure 4.1, the CRNs Ra_{T1} , Ra_{T2} and Ra_{T3} respectively for LSP, PSP and IPSP increases gradually with depth ratio \hat{d} . It is observed that IPSP is most stable one and LSP is the most unstable salinity profile. Also, the graph reveals that for lower \hat{d} values the curves are diverging, indicating that the profiles are significant in fluid layer dominant composite (FLDC) system.

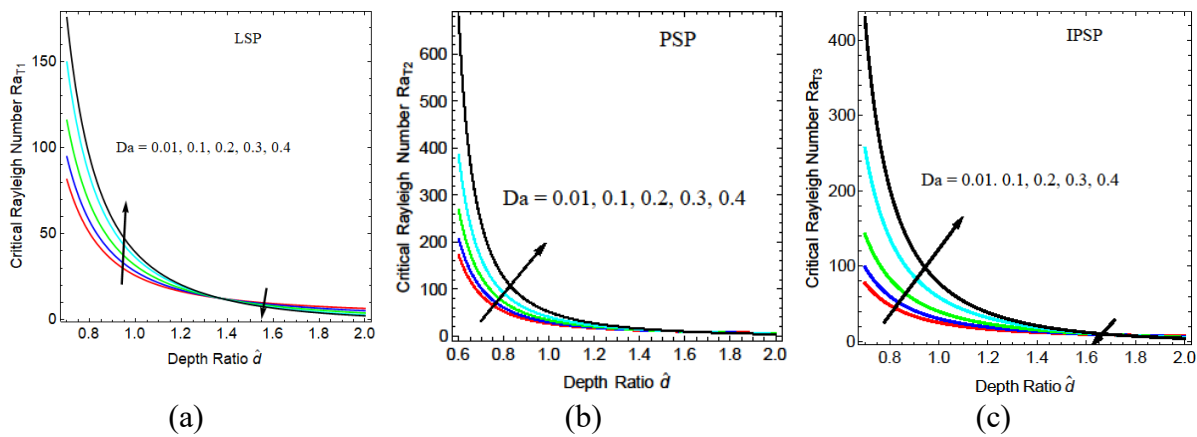


Figure 4.2: Effects of Darcy number Da

Figures 4.2a, 4.2b and 4.2c respectively shows CRN versus \hat{d} for different values of Darcy number, $Da = 0.01, 0.1, 0.2, 0.3$ and 0.4 and default values $R_i^* = R_{Im}^* = 0.5, \epsilon_T = \epsilon_s = 1, Ra_S = 5, Sr_f = Sr_m = -0.1, \tau_f = \tau_m = 0.25$. for LSP, PSP and IPSP. The CRNs Ra_{T1}, Ra_{T2} and Ra_{T3} increase with increase in Da . The graphs exhibit dual effect, that is, for smaller \hat{d} values, the system is stabilized and for larger values of \hat{d} the system is destabilized. That is, the onset of DDRB convection can be delayed or hastened depending on the range of depth ratio, \hat{d} .

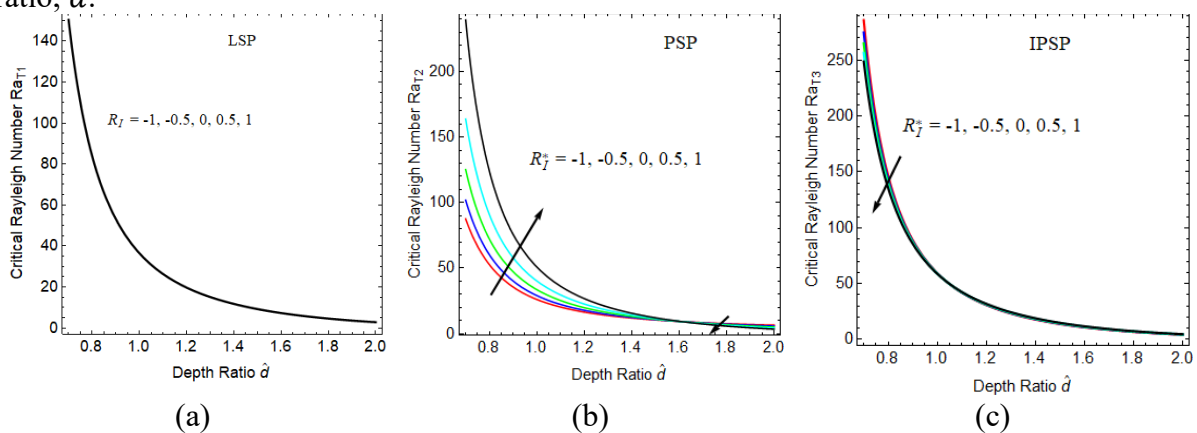


Figure 4.3: Effects of modified fluid internal Rayleigh number R_i^*

Figures 4.3a, 4.3b and 4.3c illustrates the CRN versus \hat{d} for LSP, PSP and IPSP by varying modified fluid internal Rayleigh number, $R_i^* = -1, -0.5, 0, 0.5, 1$ and the parameters $R_{Im}^* = 0.5, Da = 0.3, \epsilon_T = \epsilon_s = 1, Ra_S = 5, Sr_f = Sr_m = -0.1, \tau_f = \tau_m = 0.25$ are unaltered. No effect is observed in case of LSP. In case of PSP, a dual effect is observed. For $0 \leq \hat{d} \leq 1.66$, the system is stabilized, delaying the onset of DDRB convection, and for $\hat{d} \geq 1.66$, the system is destabilized, hastening the onset of DDRB convection. In case of IPSP, increase in R_i^* decreases CRN showing destabilizing effect and hastening the onset of DDRB convection.

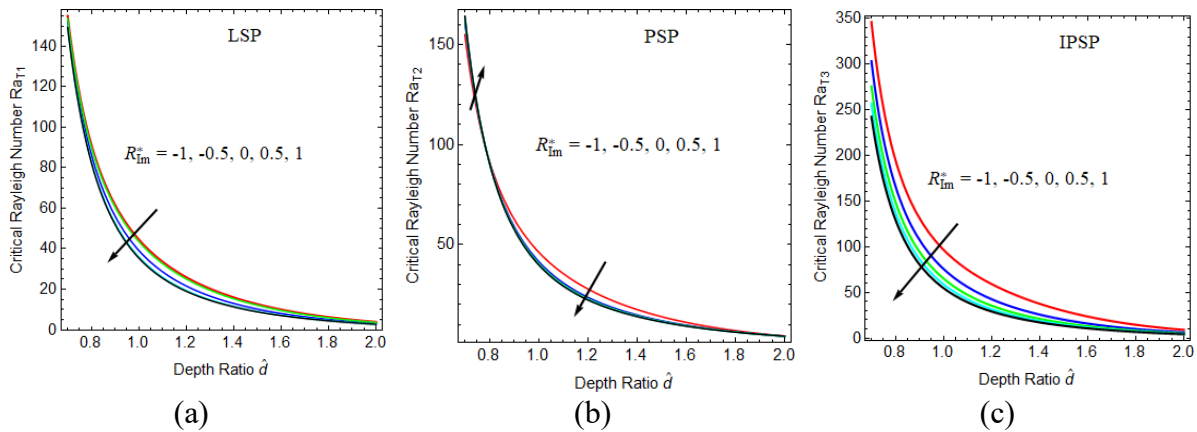


Figure 4.4: Effects of modified porous internal Rayleigh number R_{Im}^*

Figures 4.4a, 4.4b and 4.4c illustrates the CRN versus \hat{d} for LSP, PSP and IPSP by varying modified porous internal Rayleigh number, $R_{Im}^* = -1, -0.5, 0, 0.5, 1$ (increasing from sink to source) and unaltered parameters $R_I^* = 0.5, Da = 0.3, \epsilon_T = \epsilon_S = 1, Ra_S = 5, Sr_f = Sr_m = -0.1, \tau_f = \tau_m = 0.25$. In case of LSP, the curves are converging for lower and higher values of \hat{d} indicating that R_{Im}^* is prominent in the midrange of \hat{d} . A dual effect is observed in case of PSP, i.e., for lower \hat{d} values, the system is stabilized and for higher values of \hat{d} , the system is destabilized. In case of IPSP, the system is destabilized hastening the onset of DDRB convection.

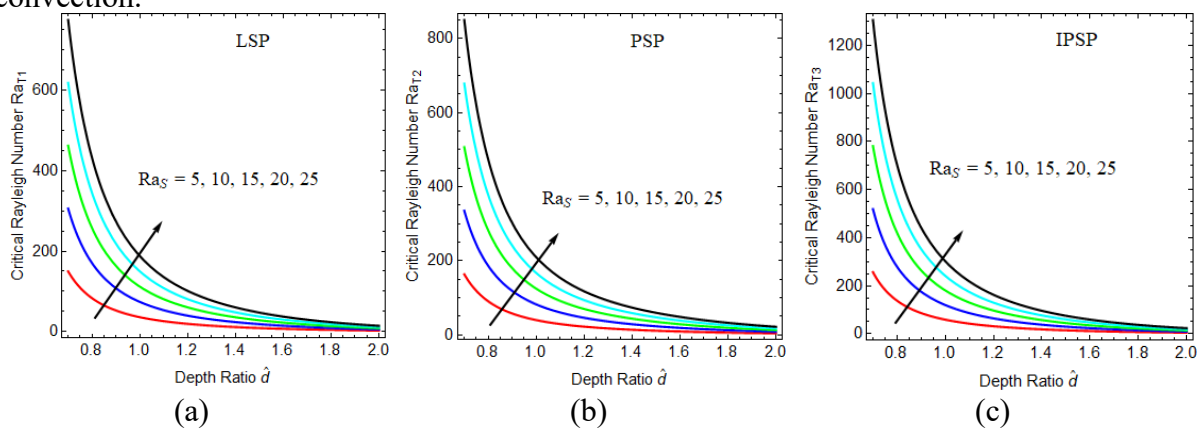


Figure 4.5: Effects of Solute Rayleigh number in fluid layer Ra_S

Figures 4.5a, 4.5b and 4.5c illustrates the CRN versus \hat{d} for LSP, PSP and IPSP by varying Solute Rayleigh number in the fluid layer, $Ra_S = 5, 10, 15, 20, 25$, and the fixed parameters $R_I^* = R_{Im}^* = 0.5, Da = 0.3, \epsilon_T = \epsilon_S = 1, Sr_f = Sr_m = -0.1, \tau_f = \tau_m = 0.25$. The CRNs Ra_{T1}, Ra_{T2} and Ra_{T3} increase with increase in \hat{d} , showing stabilizing effect and delaying the onset DDRB convection. Also, the curves are converging for larger \hat{d} values indicating that this parameter is crucial in fluid layer dominant composite (FLDC) system.

Figures 4.6a, 4.6b and 4.6c illustrates the CRN versus \hat{d} for LSP, PSP and IPSP by varying Soret parameter in the fluid layer, $Sr_f = -0.3, -0.1, 0, 0.3, 0.35$ when the other physical quantities $R_I^* = R_{Im}^* = 0.5, Da = 0.3, \epsilon_T = \epsilon_S = 1, Ra_S = 5, Sr_m = -0.1, \tau_f = \tau_m = 0.25$ are fixed. Increase in Sr_f decreases CRNs Ra_{T1} and Ra_{T2} as shown in figures 4.6a and 4.6b. That is Sr_f destabilizes the composite system and hastens the onset of DDRB convection for LSP and PSP. In case of IPSP, a dual effect is observed, i.e., for $0 \leq \hat{d} \leq 1$, increase in Sr_f

increases CRN, Ra_{T3} showing stabilizing effect and for $\hat{d} \geq 1$, increase in Sr_f decreases CRN, Ra_{T3} showing destabilizing effect. This indicates that \hat{d} plays a crucial role and this parameter is sensitive to changes in \hat{d} . Therefore, by selecting suitable salinity profile and range of \hat{d} , the composite system's onset of DDRB convection can be delayed or hastened.

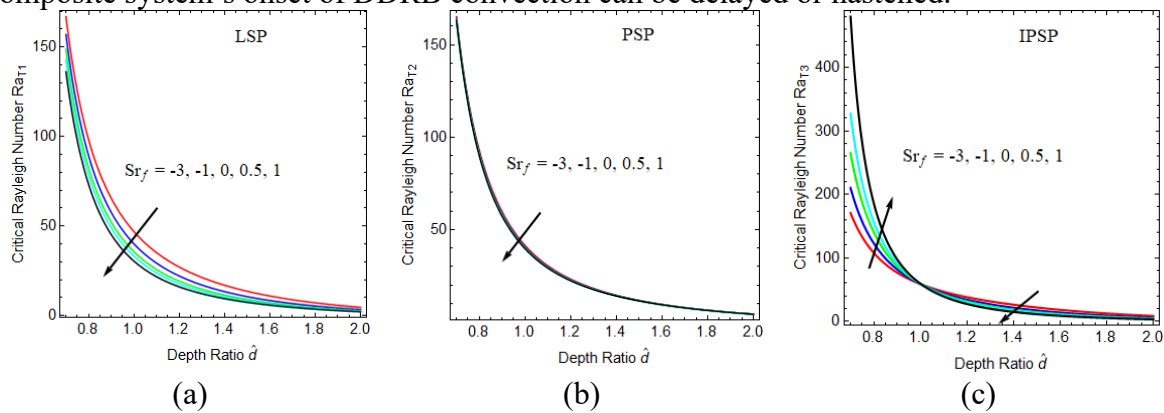


Figure 4.6: Effects of Soret parameter in fluid layer Sr_f

Figures 4.7a, 4.7b and 4.7c illustrates the CRNs, Ra_{T1} , Ra_{T2} and Ra_{T3} versus \hat{d} for LSP, PSP and IPSP by varying Solute diffusivity ratio, $\epsilon_s = 0.2, 0.4, 0.6, 0.8, 1$ and the parameters $R_l^* = R_{lm}^* = 0.5$, $Da = 0.3$, $\epsilon_T = 1$, $Ra_s = 5$, $Sr_f = Sr_m = -0.1$, $\tau_f = \tau_m = 0.25$ are default. It is observed that as ϵ_s increases, the CRNs Ra_{T1} , Ra_{T2} and Ra_{T3} decrease showing destabilizing effect and hence hastening the onset of DDRB convection for LSP, PSP and IPSP. Further, the curves are converging for larger values of \hat{d} indicating that ϵ_s is significant in FLDC system.

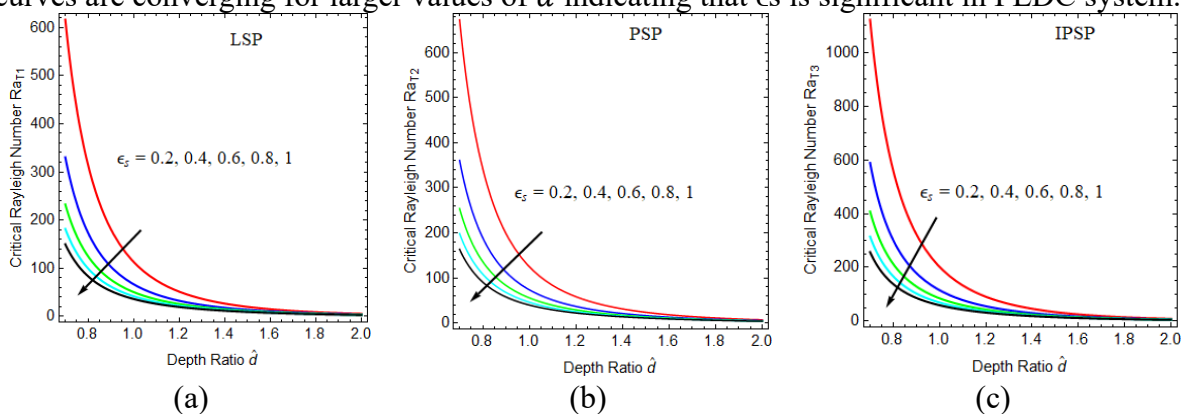


Figure 4.7: Effects of solute diffusivity ratio ϵ_s

Figures 4.8a, 4.8b and 4.8c illustrates the CRNs Ra_{T1} , Ra_{T2} and Ra_{T3} versus \hat{d} for LSP, PSP and IPSP by varying thermal diffusivity ratio, $\epsilon_T = 0.2, 0.4, 0.6, 0.8, 1$ and unaltered physical quantities $R_l^* = R_{lm}^* = 0.5$, $Da = 0.3$, $\epsilon_s = 1$, $Ra_s = 5$, $Sr_f = Sr_m = -0.1$, $\tau_f = \tau_m = 0.25$. It is observed that as ϵ_T increases the CRNs Ra_{T1} , Ra_{T2} and Ra_{T3} decrease, showing destabilizing effect and hence the onset of DDRB convection occurs faster for LSP, PSP and IPSP. Also, the curves are converging for larger values of \hat{d} indicates that ϵ_T is significant in FLDC system.

Figures 4.9a, 4.9b and 4.9c illustrates the CRNs Ra_{T1} , Ra_{T2} and Ra_{T3} versus \hat{d} for LSP, PSP and IPSP by varying solute to thermal diffusivity ratio in fluid layer, $\tau_f = 0.2, 0.4, 0.6, 0.8, 1$ and $R_l^* = R_{lm}^* = 0.5$, $Da = 0.3$, $\epsilon_T = \epsilon_s = 1$, $Ra_s = 5$, $Sr_f = Sr_m = -0.1$, $\tau_m = 0.25$ are unaltered. It is observed that as τ_f increases, the CRNs Ra_{T1} , Ra_{T2} and Ra_{T3} decrease showing destabilizing effect and hence the onset of DDRB convection occurs faster for LSP, PSP and

IPSP. In addition, the curves are diverging for lower values of \hat{d} indicating that this parameter is substantial in FLDC system.

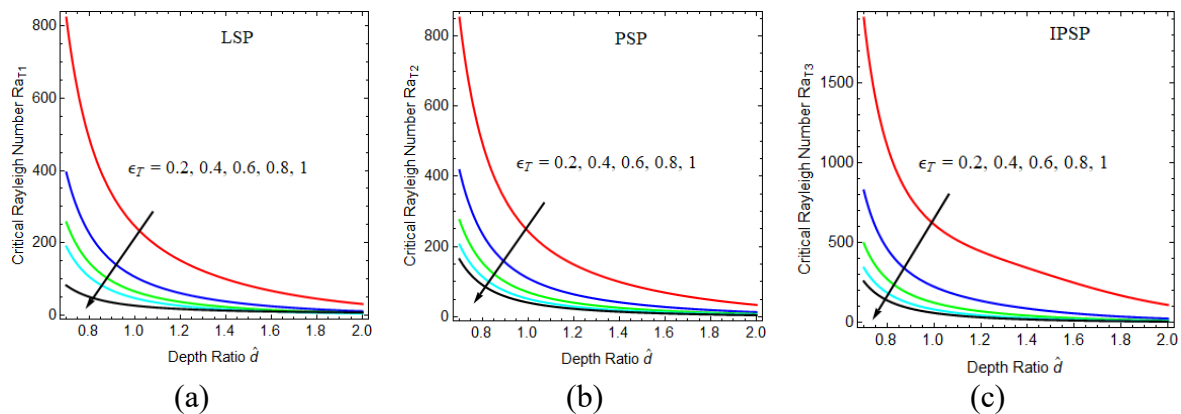


Figure 4.8: Effects of solute diffusivity ratio ϵ_T

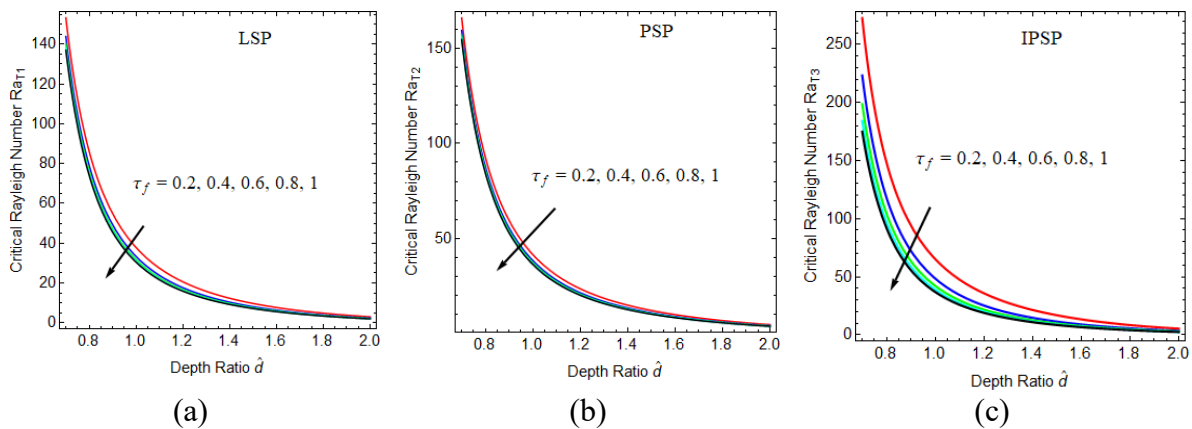


Figure 4.9: Effects of solute to thermal diffusivity ratio in fluid layer τ_f

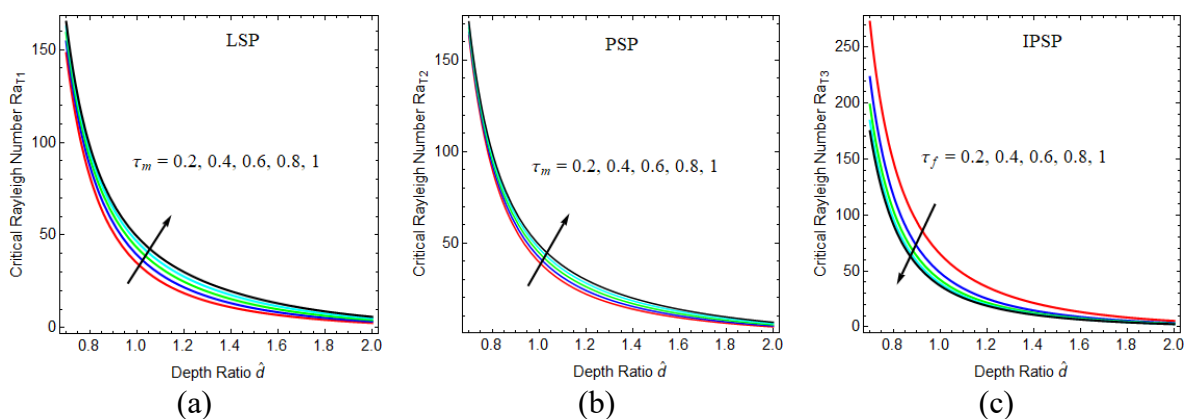


Figure 4.10: Effects of solute to thermal diffusivity ratio in porous layer τ_m

Figures 4.10a, 4.10b and 4.10c illustrates the CRNs Ra_{T1} , Ra_{T2} and Ra_{T3} versus \hat{d} for LSP, PSP and IPSP by varying solute to thermal diffusivity ratio in porous layer, $\tau_m = 0.2, 0.4, 0.6, 0.8, 1$ and $R_l^* = R_{lm}^* = 0.5, Da = 0.3, \epsilon_T = \epsilon_s = 1, Ra_s = 5, Sr_f = Sr_m = -0.1, \tau_m = 0.25$ are unaltered. It is observed that as τ_m increases the CRNs Ra_{T1} , Ra_{T2} and Ra_{T3} increase showing stabilizing effect and hence the onset of DDRB convection is delayed for

LSP, PSP and IPSP. Also, the curves are converging for lower and higher values of \hat{d} indicating that this parameter is sensitive in the mid-range of \hat{d} values.

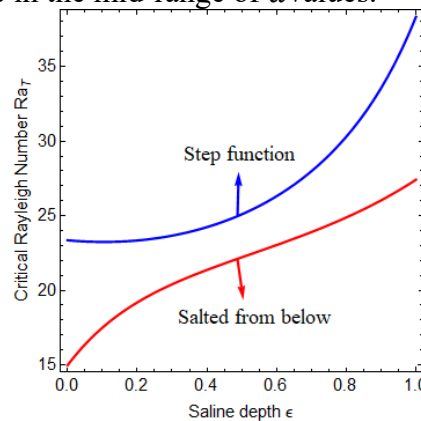


Figure 4.11: Comparison of Salted from below (SFB) and Step function (SF) salinity profiles

Figure 4.11 illustrates the comparison of Salted from below (SFB) and Step function (SF) salinity profiles. In both the profiles, the curves rise with saline depth. Also, the graph reveals that Step function is the most stable one and Salted from below is the most unstable salinity profile.

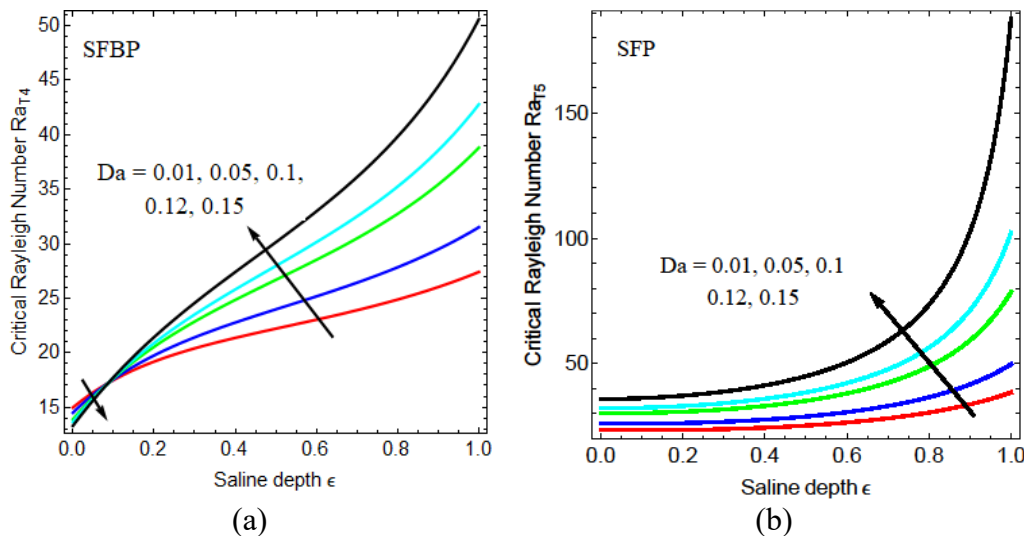


Figure 4.12: Effects of Darcy number Da

Figures 4.12a and 4.12b illustrates the CRNs Ra_{T4} and Ra_{T5} versus Saline depth, ϵ for SFBP and SFP by varying Darcy number, $Da = 0.01, 0.05, 0.1, 0.12, 0.15$. The curves rise with saline depth ϵ . In case of SFB profile, the Darcy number initially destabilizes the composite system for very small range of saline depth, i.e., $0 \leq \epsilon \leq 0.1$ and for $\epsilon \geq 0.1$, the Darcy number stabilizes the composite system. In case of SFP, increase in Da increases CRN, Ra_{T5} showing stabilizing effect and thus delaying the onset of DDRB convection. As Da increases, the flow becomes more dominated by fluid motion rather than resistance by porous medium. This enhanced fluid motion improves mixing and diffusion, reducing concentration gradients that drive convection, thus stabilizing convection and suppressing large-scale convective motion.

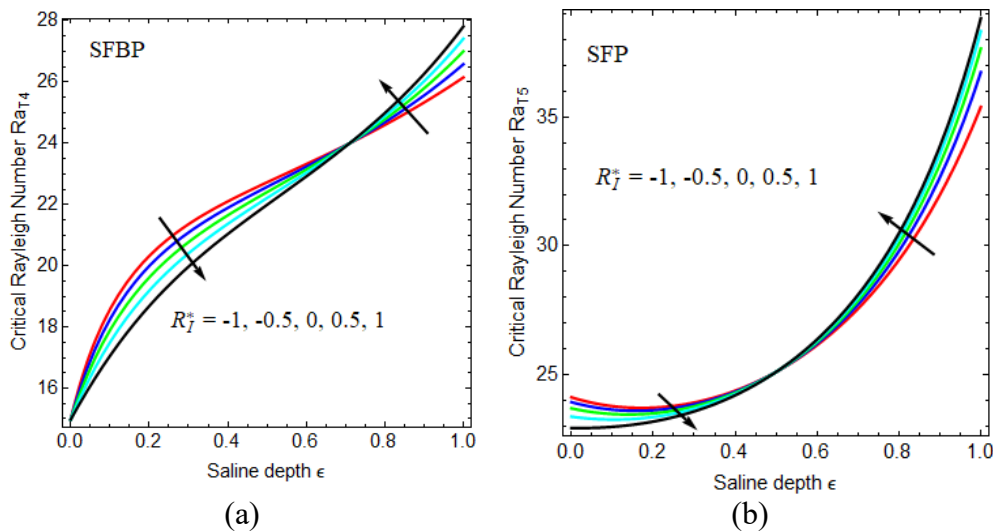


Figure 4.13: Effects of modified internal Rayleigh number in fluid layer R_I^*

Figures 4.13a and 4.13b illustrates the CRNs Ra_{T4} and Ra_{T5} versus Saline depth for Salted from below and Step function salinity profiles by varying modified internal Rayleigh number in fluid layer (from sink to source), $R_I^* = -1, -0.5, 0, 0.5, 1$. Both SFBP and SFP exhibit dual effects. In case of SFBP, the system is destabilized in $0 \leq \epsilon \leq 0.7$ and for $\epsilon \geq 0.7$, the system is stabilized. Similarly, in case of SFP, the system is destabilized in $0 \leq \epsilon \leq 0.5$ and for $\epsilon \geq 0.5$, the system is destabilized. Therefore, this parameter is sensitive to saline depth, that is, the onset of DDRB convection can be hastened or delayed depending on the range of saline depth.

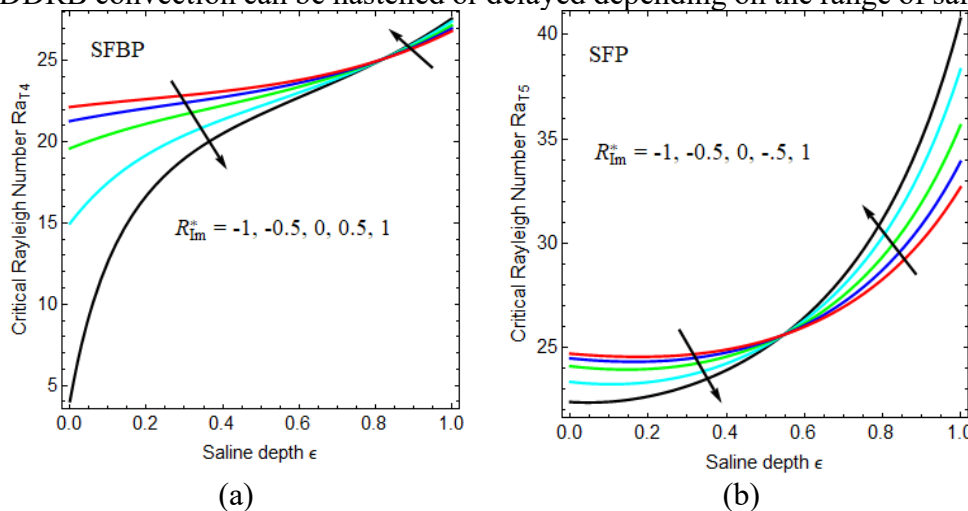


Figure 4.14: Effects of modified internal Rayleigh number in fluid layer R_{Im}^*

Figures 4.14a and 4.14b illustrates the CRNs Ra_{T4} and Ra_{T5} versus Saline depth for SFBP and SFP by varying modified porous internal Rayleigh number (from sink to source), $R_I^* = -1, -0.5, 0, 0.5, 1$. Both the graphs exhibit dual effect. In case of SFBP, the system is destabilized in $0 \leq \epsilon \leq 0.82$ and for $\epsilon \geq 0.82$, the composite system is stabilized. Similarly, in case of SFP, the system is destabilized in $0 \leq \epsilon \leq 0.55$ and for $\epsilon \geq 0.55$, the composite system is stabilized. Thus, the onset of DDRB convection can be augmented or suppressed by varying the range of saline depth.

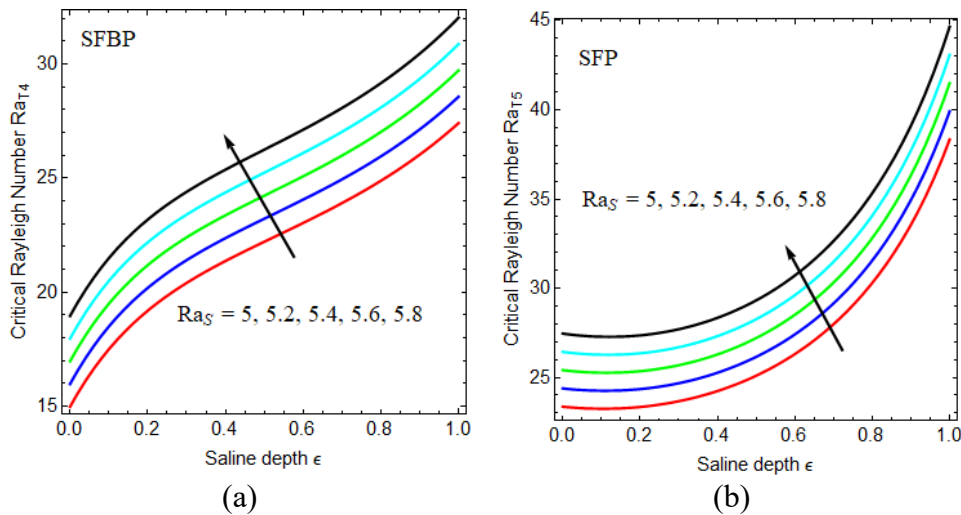


Figure 4.15: Effects of Solute Rayleigh number in fluid layer Ra_s

The plots 4.15a and 4.15b illustrates the CRNs Ra_{T4} and Ra_{T5} versus saline depth for SFBP and SFP by varying solute Rayleigh number in fluid layer, $Ra_s = 5, 5.2, 5.4, 5.6, 5.8$. The curves rise with saline depth ϵ . Higher Ra_s values (moving from red to black curves), results in higher, Ra_{T4} and Ra_{T5} indicating a stabilizing effect. Thus, the composite system is stabilized and the onset of DDRB convection is delayed. Further, the curves show a monotonic increase in CRNs as saline depth increases from 0 to 1. This indicates that as the saline layer becomes thicker, the system requires a higher thermal driving force to trigger convection, thus showing stabilizing effect.

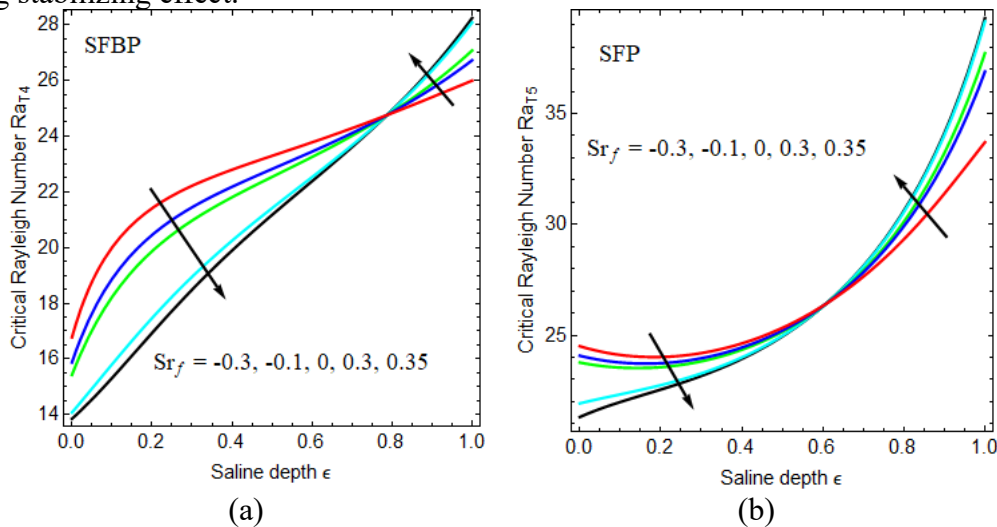


Figure 4.16: Effects of Soret parameter in fluid layer Sr_f

Figures 4.16a and 4.16b illustrates the CRNs Ra_{T4} and Ra_{T5} versus saline depth for SFBP and SFP by varying Soret parameter in fluid layer, $Sr_f = -0.3, -0.1, 0, 0.3, 0.5$. Both the profiles exhibit dual effect. In case of SFB profile, the system is destabilized in $0 \leq \epsilon \leq 0.8$ and for $\epsilon \geq 0.8$, the system is stabilized. similarly, in case of SF salinity profile, the system is destabilized in $0 \leq \epsilon \leq 0.6$ and for $\epsilon \geq 0.6$, the system is destabilized. Therefore, this parameter is sensitive to saline depth, that is, the onset of DDRB convection can be hastened or delayed depending on the thickness of saline depth. That is, both the profiles enhance density stratification, making it harder for convection to occur as the saline layer thickens.

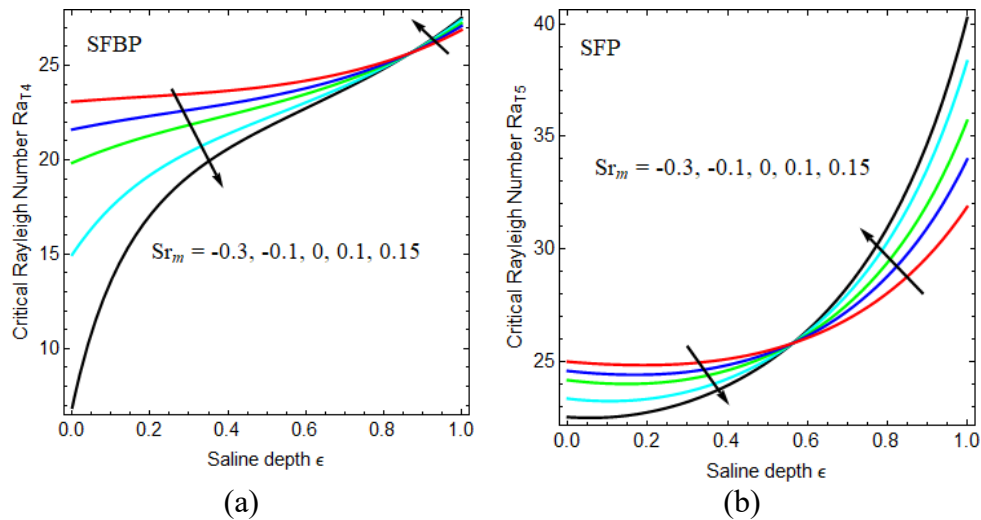


Figure 4.17: Effects of Soret parameter in fluid layer Sr_m

Figures 4.17a and 4.17b illustrates the CRNs Ra_{T4} and Ra_{T5} versus saline depth for SFBP and SFP by varying Soret parameter in porous layer, $Sr_m = -0.3, -0.1, 0, 0.1, 0.15$. Both the salinity profiles exhibit dual effects. In case of SFBP, the system is destabilized in $0 \leq \epsilon \leq 0.87$ and for $\epsilon \geq 0.87$, the system is stabilized. similarly, in case of Step function salinity profile, the system is destabilized in $0 \leq \epsilon \leq 0.56$ and for $\epsilon \geq 0.56$, the system is destabilized. At $\epsilon = 0.56$, the curves intersect, highlighting a transition zone where the Soret effect shifts from weak to strong influence.

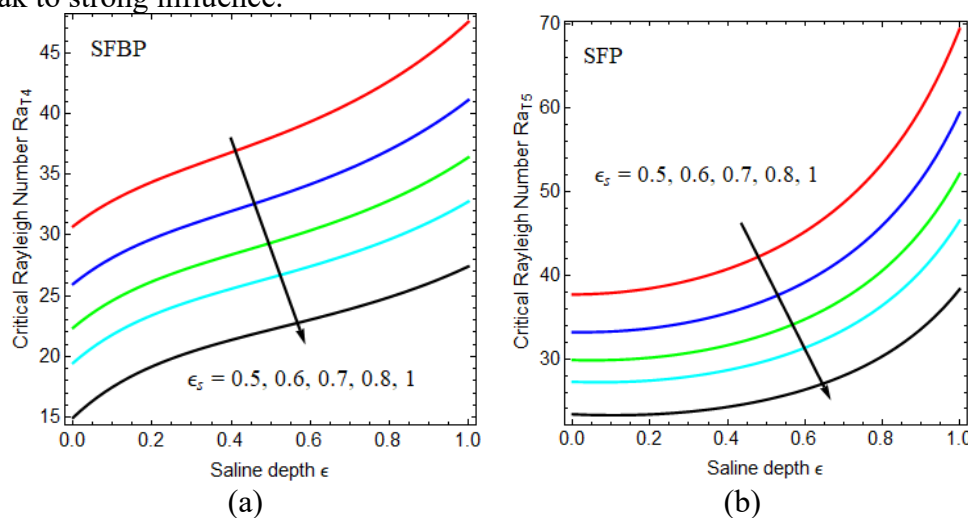


Figure 4.18: Effects of solute diffusivity ratio ϵ_s

Figures 4.18a and 4.18b illustrates the CRNs Ra_{T4} and Ra_{T5} versus saline depth for Salted from below and Step function salinity profiles by varying solute diffusivity ratio in, $\epsilon_s = 0.5, 0.6, 0.7, 0.8, 1$. As ϵ_s increases, the CRNs, Ra_{T4} and Ra_{T5} decrease showing destabilizing effect, implying that less thermal energy is required to trigger the DDRB convection.

5 Conclusion

1. The Inverted parabolic salinity profile is the most stable one and linear salinity profile is the most unstable salinity profile.

2. The parameters R_I^* , R_{Im}^* , Ra_S , τ_f and τ_m are crucial in porous dominant composite system.
3. The parameters Ra_S and τ_m stabilizes the composite system, delaying the onset of DDRB convection.
4. The Soret parameter in the fluid layer Sr_f destabilizes the system for Linear and Parabolic salinity profiles, whereas stabilizes the system for Inverted Parabolic salinity profile. For inverted parabolic salinity profile, the onset of DDRB convection can be delayed or hastened depending on the range of the depth ratio.
5. The Soret parameter in the porous layer Sr_m is also depth ratio sensitive. That is, depending on the range of the depth ratio, the onset of convection can be suppressed or augmented.
6. The strength of heat source (sink) in the fluid layer represented by modified internal Rayleigh number R_I^* shows destabilizing effect of the composite system for Inverted Parabolic salinity profile, dual effect for Parabolic salinity profile and no effect for Linear salinity profile.
7. The step function salinity profile is the most stable one and Salted from below salinity profile is the most unstable salinity profile.
8. Solute Rayleigh number, Ra_S is destabilizing the composite system for both Salted from below and Step function salinity profiles, whereas Darcy number is stabilizing the system only for step function salinity profile.
9. The parameters R_I^* , R_{Im}^* , Sr_f , Sr_m and Da (only for SFB profile) exhibit dual effect. That is, these parameters are sensitive to saline depth.
10. By varying the thickness of the saline depth, the onset of DDRB convection can be augmented or delayed.

References

- [1] Al-Qurashi, M. S. (2012). A study of salt-finger convection in a nonlinear magnetofluid overlying a porous layer affected by rotation. *Int. J. Mech. Mech*, 12, 32-40.
- [2] Ames, K. A., & Straughan, B. (1990). Penetrative convection in fluid layers with internal heat sources. *Acta mechanica*, 85(3), 137-148.
- [3] Altawallbeh, A., Bhadauria, B. S., & Hashim, I. (2018). Linear and nonlinear double-diffusive convection in a saturated porous layer with Soret effect under local thermal non-equilibrium model. *Journal of Porous Media*, 21(13).
- [4] Caldwell, D. R. (1976). Thermosolutal convection in a solution with large negative Soret coefficient. *J. Fluid Mech.* 74, 129-142.
- [5] Chamkha, A. J. (2002). Double-diffusive convection in a porous enclosure with cooperating temperature and concentration gradients and heat generation or absorption effects. *Numerical Heat Transfer: Part A: Applications*, 41(1), 65-87.
- [6] Chen, F. (1992). Salt-finger instability in an anisotropic and inhomogeneous porous substrate underlying a fluid layer. *Journal of applied physics*, 71(10), 5222-5236.
- [7] Chen, F., & Lu, J.W. (1991). Influence of viscosity variation on salt-finger instability in a fluid layer, a porous layer, and their superposition. *Journal of applied physics*, 70(8), 4121-4131.
- [8] Chen, F., & Chen, C. F. (1988). Onset of finger convection in a horizontal porous layer underlying a fluid layer. *J. Heat Transfer*, 110(2): 403-409.
- [9] Deepika, N. (2018). Linear and Nonlinear Stability of Double-Diffusive Convection with the Soret Effect. *Transp Porous Med* 121, 93-108.
- [10] Gangadharaiah, Y. H. (2013). Double diffusive Marangoni convection in superposed fluid and porous layers. *Int. J. Innovative Research Sci. Eng. Tech*, 2(7), 2625-2633.
- [11] Gangadharaiah, Y. H. (2023). Onset of double diffusive surface-tension driven convection in fluid layer overlying a layer of anisotropic porous layer with soret effect. *International Journal of Thermofluid Science and Technology*, 10(1), 100102.

- [12] Hill, A. A. (2005). Double-diffusive convection in a porous medium with a concentration based internal heat source. *Proceedings of the Royal Society A: Mathematical, Physical and Engineering Sciences*, 461(2054), 561-574.
- [13] Israel-Cookey, C., Amos, E., & Ebiwareme, L. (2018). Soret and magnetic field effects on thermosolutal convection in a porous medium with concentration based internal heat source. *American Journal of Fluid Dynamics*, 8(1), 1-6.
- [14] Kaffel Rebai, L., Mojtabi, A., Safi, M. J., & Mohamad, A. A. (2008). Numerical study of thermosolutal convection with Soret effect in a square cavity. *International Journal of Numerical Methods for Heat & Fluid Flow*, 18(5), 561-574.
- [15] Kumari, S., & Murthy, P. V. S. N. (2019). Thermosolutal convective instability of power-law fluid saturated porous layer with concentration based internal heat source and Soret effect. *The European Physical Journal Plus*, 134(9), 474.
- [16] Komala, B., & Sumithra, R. (2019). Effects of uniform and non uniform salinity gradients on the onset of double diffusive convection in a composite layer: an analytical study. *ARPN Journal of Engineering and Applied Sciences*, 14(4), 856-868.
- [17] Platten, J. K. & Chavepeyer, G. (1973). Oscillatory motion in Benard cell due to the Soret effect. *J. Fluid Mech.* 60, 305-319.
- [18] Platten, J. K. 2006 The Soret effect: a review of recent experimental results. *Trans. ASME: J. Appl. Mech.* 73, 5-15.
- [19] Rionero, S., Mulone, G. (1987). On the non-linear stability of a thermo-diffusive fluid mixture in a mixed problem. *J. Math. Anal. Appl.* 124(1), 165-188.
- [20] Shankar, B. M., Kumar, J., & Shivakumara, I. S. (2019). Stability of mixed convection in a differentially heated vertical fluid layer with internal heat sources. *Fluid Dynamics Research*, 51(5), 055501.
- [21] Straughan, B., Hutter, K. (1999). A priori bounds and structural stability for double diffusive convection incorporating the soret effect. *Proc. R. Soc. Lond. A* 455, 767-777.
- [22] Sumithra, R., Komala, B., & Manjunatha, N. (2022). The onset of Darcy-Brinkman-Rayleigh-Benard convection in a composite system with thermal diffusion. *Heat Transfer*, 51(1), 604-620.
- [23] Sumithra, R., & Komala, B. (2020). The study of effects of surface tension, magnetic field and non-uniform salinity gradients on the onset of double diffusive convection in composite system. *Malaya Journal of Matematik*, 8(03), 730-737.
- [24] Tveitereid, M. (1978). Thermal convection in a horizontal fluid layer with internal heat sources. *International Journal of Heat and Mass Transfer*, 21(3), 335-339.
- [25] Yu, C. P., & Shih, Y. D. (1980). Thermal instability of an internally heated fluid layer in a magnetic field. *Physics of Fluids*, 23(2), 411-412.
- [26] Zimmermann, G., Muller, U. & Davis, S. H. (1992). Benard convection in binary mixtures with Soret effects and solidification. *J. Fluid Mech.* 238, 657-682.